Journal of Materials Chemistry C

Polymorphism-induced multi-functional crystal photonics achieved by a highly luminescent benzofuranyl molecule having tetrafluorophenylene core

Journal:	*Journal of Materials Chemistry C*
Manuscript ID	TC-ART-02-2025-000817.R1
Article Type:	Paper
Date Submitted by the Author:	04-Apr-2025
Complete List of Authors:	Matsuo, Takumi; Kochi University of Technology, ; Hayashi, Shotaro; Kochi University of Technology, School of Environment and Engineering

ARTICLE

Polymorphism-induced multi-functional crystal photonics achieved by a highly luminescent benzofuranyl molecule having tetrafluorophenylene core

Received 00th January 20xx,
Accepted 00th January 20xx

DOI: 10.1039/x0xx00000x

Takumi Matsuo,*[a,b] and Shotaro Hayashi *[a,b]

Luminescent organic single crystals are attractive as components of miniaturized photonic integrated circuits such as optical waveguides, lasers, and optical resonators. Various functions have been discovered by designing chemical or crystal structures. The optical characteristics can be modulated by designing the crystal structures. Various polymorphic compounds have been reported, and differences in the luminescence colors have been well-explained by the differences in the crystal structures. However, drastic modulation of the photonics functions has not been reported. We report here multi-functional photonics achieved by highly luminescent and polymorphic compound 1,4-bis(benzofuran-2-yl)-2,3,5,6-tetrafluorophenylene, namely **BFTFP**. **BFTFP** exhibited three types of crystal structures: **BFTFP_*α***: flexible fiber, **BFTFP_*β***: rigid block, **BFTFP_*γ***: plate. Depending on each crystal's morphology or emission properties, we developed to assign specific photonic functions for each crystal, **BFTFP_*α***, **BFTFP_*β***, and **BFTFP_*γ***, respectively. **BFTFP_*α*** exhibited elastic flexibility with optical waveguiding. Although elastic organic single crystals tend to be less luminescent, the **BFTFP_*α*** crystal possessed 52% of Φ_{PL} which was one of the highest among previously reported elastic organic single crystals. **BFTFP_*β*** exhibited amplified spontaneous emission under excitation using a nanosecond pulsed laser due to their rigidity and monomeric luminescence. Platelet crystals of **BFTFP_*γ*** exhibited intense luminescence from their basal facets, which was ideal as media of highly luminant photonic devices such as vertical cavity surface emitting lasers.

Introduction

Organic electroluminescence devices relating to information technology have been well-developed in recent years. Apart from these organic electronics,[1-5] organic photonics utilizing π-conjugated molecules have been well-developed due to their efficient energy transports or fast responses. Especially, organic single crystals (OSCs) are ideal media to realize photonics with high functionalities of lasers or amplified spontaneous emissions (ASEs),[6-18] cavities,[19-25] and optical self-waveguides.[26-39] Using OSCs with these functions, photonic integrated circuits (PICs) have been constructed toward practical applications. R. Chandrasekar *et al.* have constructed PICs with several components of OSCs combined using a cantilever for atomic force microscopy (AFM).[26] Moreover, large-scale integrations (LSIs) of OSCs with specific optical functions of lasers, cavities, or waveguiding have been constructed.[8,32]

To investigate OSC-based photonics, highly luminescent molecules have been developed so far. *trans,trans*-1,4-Distyrylbenzenes (**DSB**) and these derivatives are frequently utilized molecules exhibiting highly luminescent performance in the solid state.[6] The molecules composed of phenylene-vinylene structures such as DSBs are one of the most utilized molecular structures to develop organic lasers. Recently, to increase the stability of the molecules composed of phenylene-vinylene structures, a bridging strategy by carbon or oxygen atoms has been proposed.[40,41] According to such strategies, unexpected events in molecules of OSCs such as *cis-trans* isomerizations or [2+2] cycloadditions in the vinylene structures can be prevented.[40,42,43]

Not only the chemical structure but also the molecular aggregation states also determine the optoelectronic characteristics of OSCs. To rationally develop the optoelectronic performance, crystal structures in terms of molecular conformation, packing, or alignments must be considered. Takimiya *et al.* have developed crystal engineering for the improvement of OSC transistors.[3] To develop the photonic functions of OSCs, polymorphism has been efficiently utilized. Polymorphism is sometimes regarded as disadvantageous contamination properties because several types of crystals were unexpectedly mixed; thus, crystals with various properties were included in one batch. However, this contamination is not disadvantageous in the case of OSC μ-photonics since only one isolated OSC is utilized in the demonstration.[7,16] Furthermore, the utilization of polymorphism can be a good methodology for the development of OSCs because the probability of the appearance of OSCs with high performance is increased.

Although the rational designing toward the appearance of polymorphism is still challenging, design strategy has been

[a] School of Engineering Science, Kochi University of Technology, Kami, Kochi 782-8502, Japan.
[b] FOREST Center, Research Institute, Kochi University of Technology, Kami, Kochi 782-8502, Japan.

gradually constructed recently. Polymorphs are roughly categorized into packing polymorphs or conformation polymorphs. 5-Methyl-2-[(2-nitrophenyl)amino]thiophene-3-carbonitrile; called **ROY** is known as one of the most polymorphic compounds. The origin of the polymorphism was interpreted as the movability of the molecular conformation, which was categorized as conformational polymorphism.[41] Additionally, various intermolecular hydrogen bonding patterns can also induce polymorphism, which was categorized as packing polymorphism.[45-47]

Here, we designed 1,4-bis(benzofuran-2-yl)-2,3,5,6-tetrafluorophenylene, namely **BFTFP**, as a highly luminescent and polymorphic compound toward polymorphism-based OSC photonics.[48] First of all, as a highly luminescent moiety and optically robust structure, **BFP**, an oxygen-bridged DSB structure, was designed as depicted in Scheme S1. Additionally, to induce the packing polymorphism in **BFP**, we introduced fluorine atoms into the central phenylene unit as displayed in Chart 1. The partially introduced hetero-atoms or halogen atoms could contribute to inducing the multi-intermolecular hydrogen bonding, resulting in packing polymorphism. Furthermore, we examined the relative energy at each torsion angle for the simplified chemical structure of **BFTFP** (Scheme S2). According to the literature, the conformation with the relative energy below *ca*. 5 kJ/mol is allowed to appear.[49,50] Based on this fact, the torsion angle between the central phenylene unit and benzofuran unit; ϑ_t below 45° was expected to appear. Thus, conformational polymorphism due to this torsion movability can also be expected. In this work, we created polymorphs of **BFTFP** and achieved multi-functional photonics in terms of optical waveguiding, lasers, and optical resonators based on the polymorphisms in **BFTFP**.

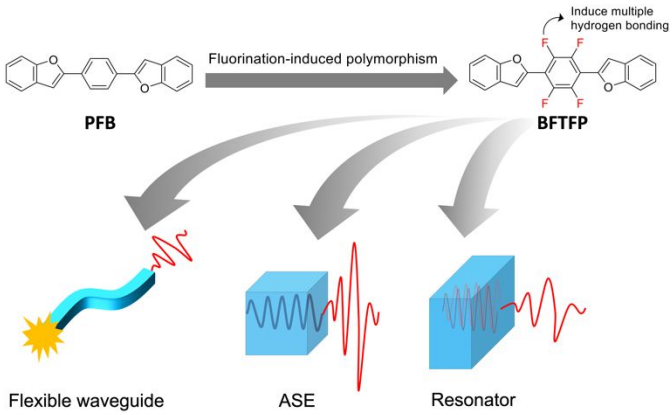

Chart 1. Schematic depiction of chemical structure designing strategy for polymorphism-based multi-photonics.

Results and Discussion

As shown in Scheme 1, **BFTFP** was synthesized via Suzuki-Miyaura cross-coupling reaction of 1,4-dibromotetrafluorobenzene with benzofuran-2-boronic acid in 37 % yield. The target compound **BFTFP** was identified by measurements of ^{1}H-NMR, ^{13}C-NMR, spectra, and high-resolution mass-spectroscopy (HR-MS) (Figs S1-S3).

Scheme 1. Synthesis of **BFTFP**.

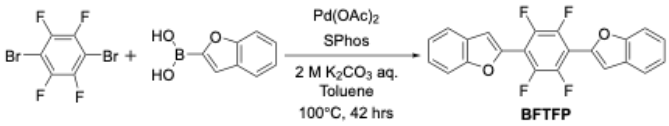

To yield polymorphs of **BFTFP**, three types of growth processes were performed. Each methodology was schematically displayed in Fig. 1. Figs 1a-1c exhibit a schematic depiction of solvent diffusion, vapor diffusion, and sublimation processes, respectively. The detailed procedures are described in the Experimental section. As a result of the crystal growth, three crystal morphologies were discovered. In all processes, crystals with fiber morphology, and mechanical flexibility were yielded. By solvent diffusion process, fiber crystals were obtained as sole morphology. In the case of the vapor diffusion process, crystals with block morphology grown on the glass plates contained in the petri dish were obtained. By sublimation process, platelet crystals were obtained. The obtained crystal morphology was named **BFTFP_*α*** for the fiber crystals, **BFTFP_*β*** for the block crystals, and **BFTFP_*γ*** for platelet crystals, respectively.

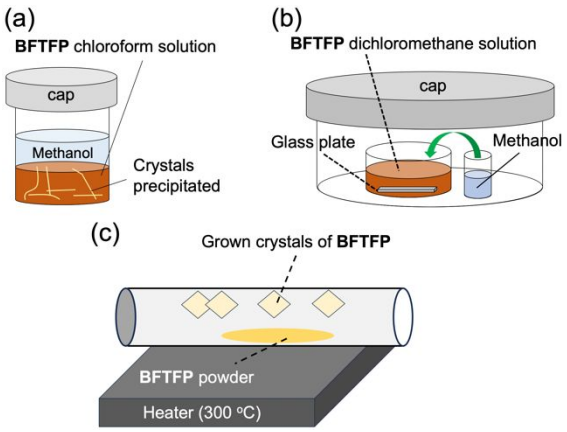

Fig. 1. Schematic illustrations of crystal growth by (a) solvent diffusion process, (b) vapor diffusion process, and (c) sublimation process.

Figs 2a-c show each fluorescence microscope image taken for **BFTFP_*α***, **BFTFP_*β***, and **BFTFP_*γ***, respectively. As the images show, each crystal exhibited drastically varied crystal morphology. Fig. 2d shows photoluminescence (PL) and its excitation (PLE) spectra measured for each crystal. Although **BFTFP_*α*** and **BFTFP_*γ*** exhibited similar broad spectra, only **BFTFP_*β*** showed drastically varied sharp PL spectrum exhibiting vibronic transitions. It suggested that luminescence from molecules in the monomeric state in the crystal of **BFTFP_*β***. Fig. S4 shows PL decay profiles measured for **BFTFP_*α*** and **BFTFP_*β***. Each decay profile was well-fitted as a 2nd-order exponential decay curve. The fitting function $f(t)$ is described as follows; $f(t) = A_1\exp(-t/\tau_1) + A_2\exp(-t/\tau_2)$ where A_1 and A_2 are constant, τ_1 and τ_2 are lifetime, and t is the decay time. For the case of **BFTFP_*α***, A_1, A_2, τ_1, and τ_2 are 0.08, 0.044, 1.79, and 4.25, respectively. The average PL lifetime (τ_{ave}) was estimated to be 2.66 ns. For the case of **BFTFP_*β***, A_1, A_2, τ_1, and τ_2, are 0.13, 0.0060, 1.06, and 2.95, respectively. τ_{ave} was estimated to be 1.14 ns. Thus,

the luminescence decay is faster for the case of **BFTFP_*β*** compared to the case of **BFTFP_*α***, which also suggested the monomeric emission for **BFTFP_*β*** rather than excimer emissions.

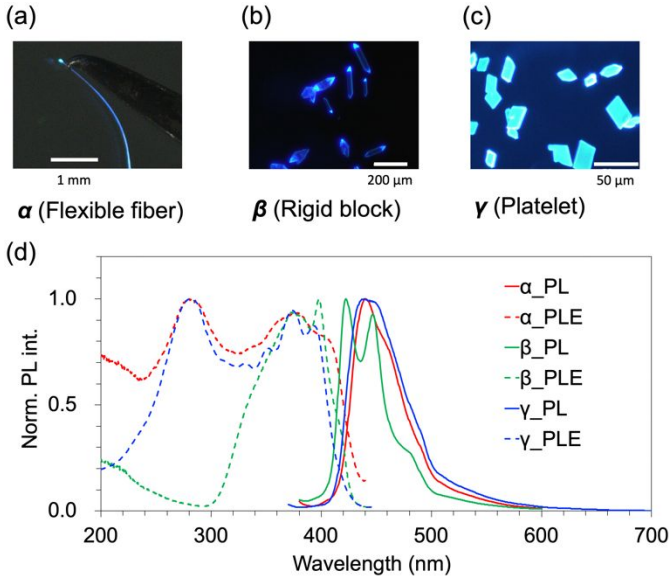

Fig. 2. Fluorescence microscope images of (a) **BFTFP_*α***, (b) **BFTFP_*β***, and (c) **BFTFP_*γ***, respectively. (d) PL and PLE spectra measured for each polymorph.

Next, crystal structures were revealed for **BFTFP_*α***, **BFTFP_*β***, and **BFTFP_*γ***, respectively. Figs 3a-3d show the crystal structure of **BFTFP_*α***. Fig. 3a shows the conformation of **BFTFP_*α***. The torsion angle estimated for the benzofuran unit to tetrafluorophenylene unit (ϑ_t) was 19.42°. Fig. 3b shows one of the packings between neighboring two molecules. Hydrogen bonding was suggested between Fluorine and hydrogen atoms. Fig. 3c shows π-π stacking suggested between two molecules packed as a face-to-face motif. Fig. 3d shows the crystal structure projected on the *bc*-plane with a schematic depiction of crystal morphology for indicating crystal long axis; *b*-axis direction. Figs 3e-3h show the crystal structure of **BFTFP_*β***. Fig. 3e shows the conformation of **BFTFP_*β***. Two conformations, namely conformation 1 and conformation 2, were contained in the crystal structure. The torsion angle ϑ_t was estimated to be 9.26-38.53°. Fig. 2f shows one of the packings between two molecules of conformation 1. Fig. 3g shows one of the packings between two molecules of conformation 2. Hydrogen bonding was suggested between fluorine and hydrogen atoms. Fig. 3h shows the crystal structure projected on the *bc*-plane with a schematic depiction of crystal morphology for indicating crystal long axis; *c*-axis direction. Figs 3i-3n show the crystal structure of **BFTFP_*γ***. Fig. 3i shows the conformation of **BFTFP_*γ***. Two conformations, namely conformation 1 and conformation 2, were contained in the crystal structure. In conformation 2, the benzofuran units were disordered. The occupancy of the main benzofuran unit was 56.2 %. The packing was displayed using the mainly occupied benzofuran units. The torsion angle ϑ_t was estimated to be 0.32°-4.82°. Fig. 3i shows one of the packings between two conformation 1. Fig. 3k shows one of the packings between two conformation 2. Compared to the cases of **BFTFP_*α*** and **BFTFP_*β***, different patterns of hydrogen bonding were suggested between fluorine and hydrogen. Fig. 3l shows crystal structure projected on the *bc*-plane with a schematic depiction of crystal morphology for indicating crystal elongation along *a*- and *b*-axis directions. In the preliminary examination, as depicted in Scheme S2, the allowed predicted torsion angles in the crystal range from 0 to *ca.* 45°. The experimentally appeared torsion angles were 0.32 - 38.53 °, among **BFTFP_*α***, **BFTFP_*β***, and **BFTFP_*γ***, which angle values were well-corresponded to the preliminary examination. Thus, it was suggested that both multiple hydrogen bonding and rotatability contributed to the appearance of polymorphs. In the crystal structures, the planar π-planes of **BFTFP_*α*** and **BFTFP_*γ*** were well-overlapped while **BFTFP_*β*** possessed highly twisted conformations and small π-plane overlapping. Figs S5-S8 show the simulated molecular orbitals, absorption spectra, and oscillator strength (*f*) of **BFTFP** obtained from time-dependent density functional theory (TDDFT) calculations using a neighboring molecule model generated by a crystal structure (CIF file). Tables S1-S4 also summarized the results of the calculations. In the result of **BFTFP_*β***, the molar absorption coefficient was larger than 17000 $M^{-1}*cm^{-1}$, which was larger than the cases of **BFTFP_*α*** and **BFTFP_*γ***. The molecular orbitals were localized, which was ideal for high luminescence performance. These properties of crystal structures were well-corresponded to the luminescence characteristics; PL spectra shape, and PL lifetime shown in Figs 2d and S4. **BFTFP_*α*** and **BFTFP_*γ*** exhibited broad excimer emission while **BFTFP_*β*** exhibited sharp monomeric emission.

Before the investigations of photonic functions for each polymorph, absolute PL quantum efficiency (Φ_{PL}) was estimated for the majorly obtained crystal form **BFTFP_*α***. The Φ_{PL} was estimated to be 0.52 (52 %), which was one of the highest values among flexible OSCs.[17] To the best of our knowledge, the pitched-π stack packing motif induces flexibility.[27] However, this motif also induces less emissive properties due to the well-overlapped π-orbitals. The high Φ_{PL} for **BFTFP_*α*** suggested that

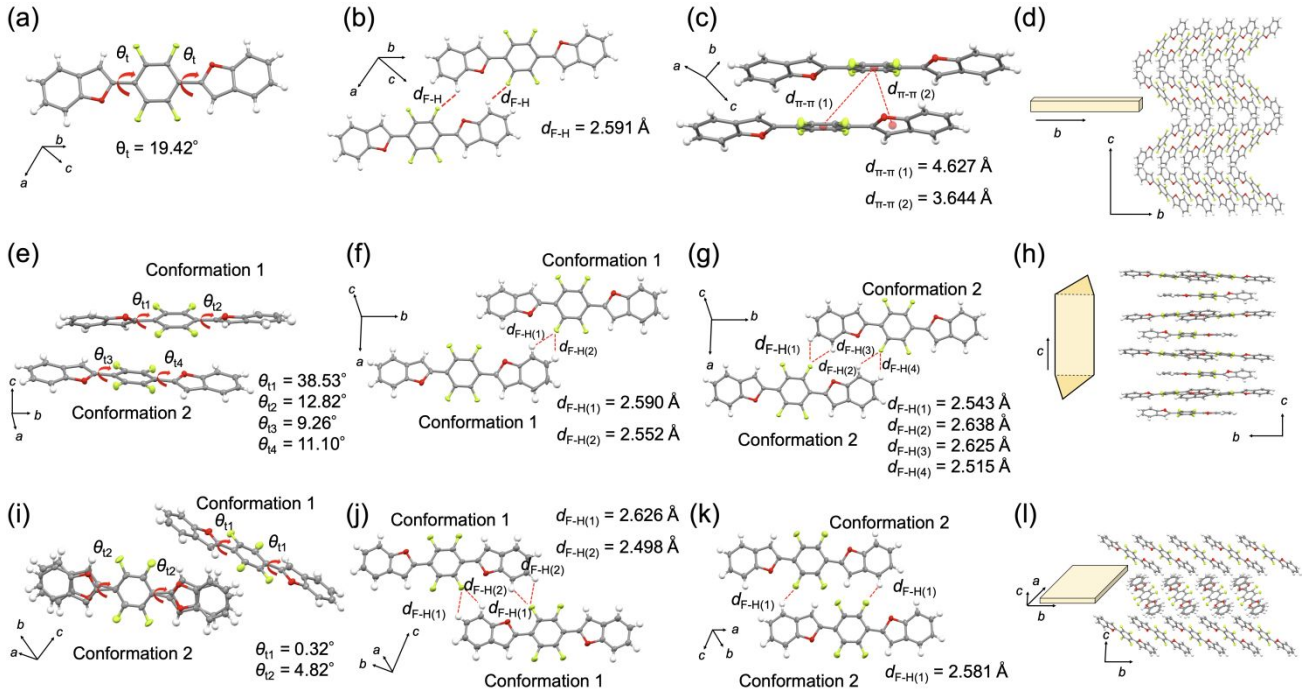

Fig. 3. Crystal structures of (a-d) **BFTFP_*α***, (e-h) **BFTFP_*β***, and (i-l) **BFTFP_*γ***, respectively.

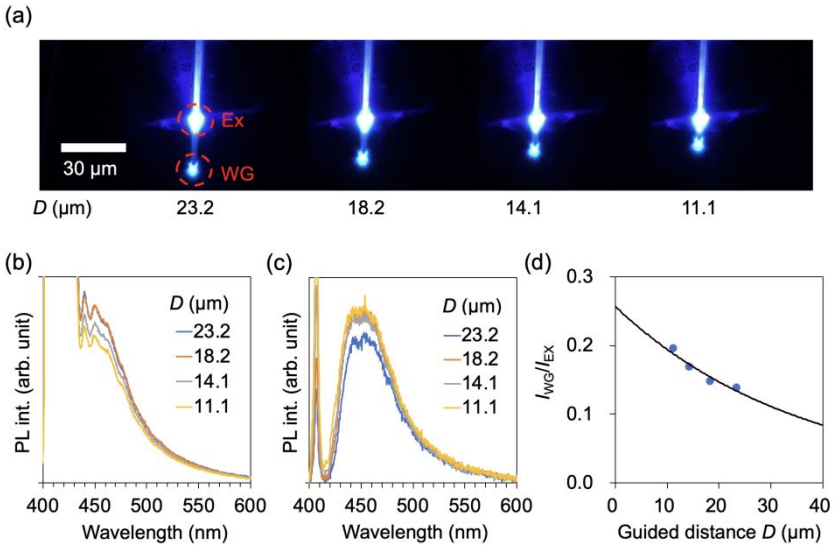

Fig. 4. Optical waveguide. (a) Fluorescent microscope images of an isolated crystal of **BFTFP_*α*** taken at different excitation positions along the crystal long axis. (b) The spatially resolved μ-PL spectra measured at excitation, Ex position. (c) The spatially resolved PL spectra measured at the edge, WG, position corresponding to the image. (d) The ratios of the intensity I_{WG}/I_{Ex} against the distance *D* correspond the image (a) with a fitting curve.

the chemical structure designed in this research worked well with high luminescence performance.

Next, we assigned specific photonic functions for **BFTFP_*α***, **BFTFP_*β***, and **BFTFP_*γ***, respectively, toward multi-functional photonics based on polymorphism. To assign a specific photonic function for **BFTFP_*α*,** fluorescence waveguiding characteristics were examined as shown in Fig. 4. In this characterization, microscopic observations and PL spectral measurements of the **BFTFP_*α*** were performed using a focused laser beam (λ_{ex} = 405 nm) as an excitation source (Set-up: Fig. S9). When the focused laser beam irradiated an isolated fiber crystal, the luminescence was guided toward the edge of the crystal. We measured the light emission at the laser irradiation position (Excitation position: Ex) and the crystal edge (Guided position: WG) as a spatially resolved PL spectrum. Spatially resolved PL spectra were measured at 4 points where the guided distance *D* was

23.2, 18.2, 14.1, and 11.1 from the excitation position to the waveguiding position along the long axis of the crystal (Fig. 4a). Figs 4b and 4c show PL spectra taken at Ex and WG at each *D*. The emission intensities at the excitation and guided positions were monitored at 470 nm as I_{Ex} and I_{WG}, respectively, and I_{WG}/I_{Ex} were plotted at each *D* (Fig. 4d). Fitting according to the function $I_{WG}/I_{EX} = A\exp(-\alpha D)$ [*A*: constant, α: loss coefficient gave α = 279 dBcm^{-1} was performed. Furthermore, bending characterizations were performed for an isolated crystal of **BFTFP_*α*** placed on a glass substrate (Fig. S10). When the mechanical stress was applied to the straight-shaped crystal using a tweezer and a metal needle, the crystal showed bending flexibility. After releasing the stress, the crystal shape returned to its straight form. Thus, the flexibility was categorized in elasticity rather than plasticity.[30]

In general, monomeric emission shows high efficiency in luminescence, which is ideal for the application of laser media.[6,12,13] With this situation in mind, ASE characteristics were examined for **BFTFP_*β*** by optical pumping using an Nd:YAG pulsed laser (λ_{ex} = 355 nm; pulse duration of ~5 ns; and repetition frequency of 1 kHz). The measurement setup is shown in Fig. S11. The PL intensity (I_{PL}) increased with increasing excitation fluence (I_{ex}) (Fig. 5a). At a lower I_{ex}, a broad PL band appeared. At a higher I_{ex} (*ca.* $\gtrsim$ 470 μJ/cm^2), a narrow band with increased intensity was observed. Fig. 5b shows the dependence of I_{ex} on the integrated PL intensity. The PL intensity increased sublinearly at a lower excitation power and superlinearly at a higher excitation power, resulting in the appearance of a threshold at 431 μJ/cm^2. The slope of the plots was estimated to be 0.8 ($I_{PL}^{0.8} \propto I_{ex}$) in the sublinear regime, while that was 1.5 ($I_{PL}^{1.5} \propto I_{ex}$) in the superlinear regime. Additionally, the band width was estimated as the full width at half maximum (FWHM), which was estimated as a result of peak fitting using the lorentian function. The band width was also dramatically sharpened appearing as a threshold. Thus, the **BFTFP_*β*** exhibited ASE with a threshold.

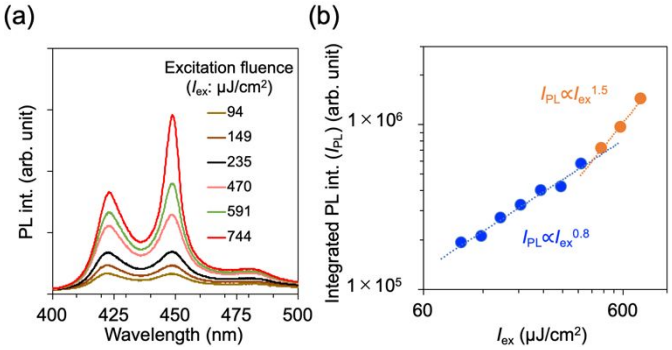

Fig. 5. PL spectra measured for an isolated **BFTFP_*β*** crystal taken at varied I_{ex} values (microjoules per square centimeter) and (b) dependence of integrated PL intensity and FWHM on the I_{ex}.

As shown in Fig. 2c, **BFTFP_*γ*** is a two-dimensional morphology. Additionally, the PL appeared from the basal facet of the crystal. This property is ideal as a media for highly luminant devices such as vertical cavity surface emitting lasers (VCSELs).[51,52] To characterize the vertical cavity properties, μ-PL measurements were performed for an isolated crystal of **BFTFP_*γ***. Fig. 6a exhibits the measurement scheme. The crystal was optically excited using an LED (λ_{ex} = 365 nm). The μ-PL spectrum was measured using a set-up as shown in Fig. S8. Interestingly, sharp optical fringes appeared in the PL spectrum (Fig. 6b; the inset shows the PL microscope image of the measurement sample). Considering the direction of PL detection, the fringes in the PL spectrum derived from the strong PL confinement, resulting in interference in the vertical direction of the crystal. The thickness (*T*) of the measured sample was estimated to be 1.2 μm using a surface profiler. Furthermore, values of group refractive indices (n_g) were estimated using the equation $n_g = 1/(2L*\Delta E)$, where *L* is the resonator length (cm) which is the same as the estimated *T*, and ΔE is the mode interval value (cm^{-1}). The n_g values were estimated to be 3.6–10 (Fig. 6c), which are high and indicate the strong confinement of photons inside the crystal. This vertical cavity in **BFTFP_*γ*** exhibiting sharp fringes and n_g values possesses potential for applications in highly luminant devices, VCSELs, or polariton laser media.[51,52]

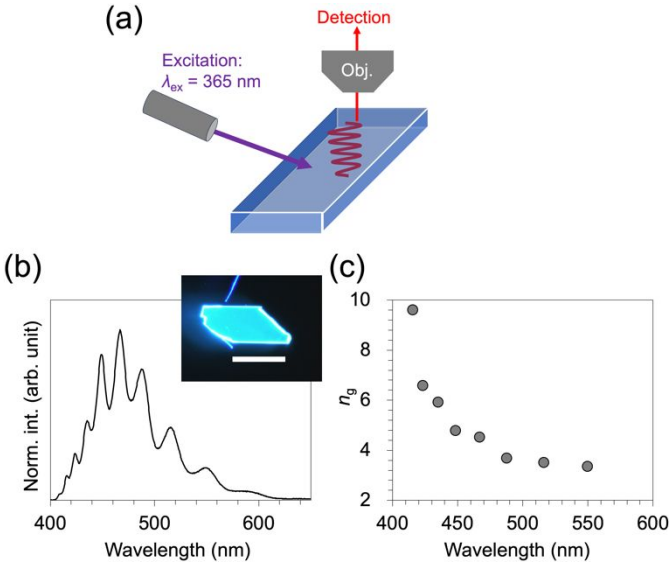

Fig. 6. (a) Schematic depiction of the μ-PL measurement. (b) PL spectrum exhibiting interference fringes. The inset shows a **BFTFP_*γ*** crystal used for the measurement. Scale bar: 500 μm. (c) Dispersion of n_g on wavelength.

To investigate the effectivity of the chemical structure designing strategy for **BFTFP**, 1,4-bis(benzothiophene-2-yl)-2,3,5,6-tetrafluorophenylene (**BTTFP**), 1,4-bis(benzofuran-2-yl)-phenylene (**BFP**) and *trans,trans*-1,4-bis(2-phenylethenyl)-2,3,5,6-tetrafluorophenylene (**PETFP**) were synthesized. Schemes S3-S5 show the synthesis scheme of **BTTFP**, **BFP**, and **PETFP** respectively. Figs S12-S14 show ^{1}H-NMR, ^{13}C-NMR spectra, and HR-MS measured for **BTTFP**, respectively. Figs S15-S17 show ^{1}H-NMR, ^{13}C-NMR spectra, and HR-MS measured for **BFP**, and Figs S18-S20 show ^{1}H-NMR, ^{13}C-NMR spectra, and HR-MS measured for **PETFP**, respectively. To obtain single crystals, growth processes depicted in Figs 1a-1c, the same as the case of **BFTFP** were also performed for **BTTFP** and **BFP**, **PETFP** respectively. As a result, **BTTFP** was crystallized in flexible fiber

morphology as well as **BFTFP_α**, in any cases. Fig. S21 shows the crystal structure of **BTTFP**. The benzothiophene unit exhibited disorder based on the rotation. The major occupancy was 61.1 %. As Fig. S21a shows, the torsion angle estimated for the benzothiophene unit to tetrafluorophenylene unit (ϑ_t) was estimated to be 3.69°. In Fig. S21b, π-π stacking was suggested between face-to-face stacked molecules. In the different molecular interactions, hydrogen bonding was suggested between fluorine and hydrogen as shown in Fig. S21c. Fig. S21d shows the crystal structure projected on the *bc*-plane with a schematic depiction of crystal morphology for indicating the crystal's long axis; *b*-axis direction. The packing motif was categorized in pitched-π stacking. Fig. S22 shows the PL and PLE spectra measured for **BTTFP** crystals. One broad PL spectrum appeared suggesting the excimer formation in luminescence. Thus, **BTTFP** crystals exhibited similar packing, and luminescence properties to the case of **BFTFP_α**. Fig. S23 and Table S4 show the results of TDDFT calculation for a model of face-to-face stacked **BTTFP** crystal. The *f* value was smaller than that those of **BFTFP_α**. Fig. S25 shows PL lifetime measured for the crystals of **BTTFP**. The profile was well-fitted as a 2nd-order exponential decay curve where A_1, A_2, τ_1, and τ_2, are 0.060, 0.040, 0.56, and 1.40, respectively. Φ_{PL} of crystals of **BTTFP** was estimated to be 0.18. The radiative rate constant (k_r) was calculated to be 0.19 ns^{-1} using an equation: $k_r = \Phi_{PL}/\tau_{PL}$. The nonradiative rate constant (k_{nr}) was calculated to be 0.88 ns^{-1} using an equation: $k_{nr} = (1-\Phi_{PL})/\tau_{PL}$. Similarly, k_r and k_{nr} were estimated for **BFTFP_α**, resulting in k_r = 0.20 ns^{-1}, k_{nr} = 0.18 ns^{-1}, respectively. In the comparison of luminescence characteristics between crystals of **BFTFP_α** and **BTTFP**, the k_r values were almost the same as each other. However, k_{nr} of **BFTFP_α** was drastically smaller than the case of **BTTFP** crystals derived from the heavy atom effect of the sulfur atom in the comparison to the oxygen atom,[53-55] and suggested the effectivity of Oxygen atom bridging strategy as depicted in Scheme S1.

To examine the effectiveness of the fluorination strategy on the appearance of polymorphism, characterizations were performed for crystals of **BFP**. As a result of crystal growth, two polymorphs were obtained. The crystal grown by sublimation process was named **BFP_α**, and grown by solvent diffusion or vapor diffusion process was named **BFP F_β**. Figs S25a-S25d shows the crystal structure of **BFP _α**. Fig. S25a shows the conformation of **BFP_α**. The torsion angle estimated for the benzofuran unit to phenylene unit (ϑ_t) was estimated to be 0.59° and 0.81°. Fig. S25b shows one of the packings between two molecules. CH-π interaction was suggested. Fig. S25c shows packing suggesting a herringbone packing motif. The herringbone angle was estimated to be 51.70°. Fig. S25d shows crystal structure projected on the *bc*-plane with a schematic depiction of crystal morphology for indicating crystal elongation direction; along *a*- and *b*-axis directions. Figs S25e-S25h show the crystal structure of **BFP_β**. Fig. S25e shows the conformation of **BFP _β**. The benzofuran unit exhibited disorder based on the rotation. The major occupancy was 59.4 %. The torsion angle estimated for the benzofuran unit to phenylene unit (ϑ_t) was estimated to be 0.38-1.30°. Fig. S25f shows one of the packings between two molecules. CH-π interaction was suggested. Fig. S25g shows packing suggesting a herringbone packing motif. The herringbone angle was estimated to be 52.06°, which was quite similar to that of **BFP_α**. Fig. S25h shows crystal structure projected on the *bc*-plane with a schematic depiction of crystal morphology for indicating crystal elongation direction; along *a*- and *c*-axis direction. Figs S26a and S26b show the PL and PLE spectra measured for **BFP_α** and **BFP_β**, respectively. Each graph contains the fluorescence microscope image as an inset. The PL band exhibited vibronic transitions and showed quite similar shape each other. Although the PL spectra were similar to each other, the luminescence performance was distinct each other for **BFP_α** and **BFP_β**. Φ_{PL} was estimated to be 0.70 for **BFP_α** while that estimated for **BFP_β** was 0.30. Fig. S27 shows PL decay profiles taken for **BFP_α** and **BFP_β**, respectively. For the case of **BFP_α**, A_1, A_2, τ_1, and τ_2, are 0.110, 0.023, 2.192, and 3.807, respectively. τ_{ave} was estimated to be 2.47 ns. For the case of **BFP_β**, A_1, A_2, τ_1, and τ_2, are 0.080, 0.058, 0.710, and 2.505, respectively. τ_{ave} was estimated to be 1.46 ns. For **BFP_α**, k_r and k_{nr} were estimated to be 0.28 ns^{-1} and 0.12 ns^{-1}, respectively. For **BFP_β**, k_r and k_{nr} were estimated to be 0.21 ns^{-1} and 0.41 ns^{-1}, respectively. Although the difference in k_r values of **BFP_α** and **BFP_β** was slight, k_{nr} of **BFP_α** was drastically smaller than that of **BFP_β**. The origin of the higher Φ_{PL} estimated for **BFP_α** mainly derived from this smaller k_{nr}. Interestingly, the packing in the crystal was quite similar to each other for **BFP_α** and **BFP_β**, however, the luminescence performance was drastically different, which is going to be examined in future work. Figs S28, S29, Tables S6, and S7 show the results of TDDFT calculation. As supporting the difference of the Φ_{PL}, *f* of **BFP_α** was larger than that of **BFP_β**. **BFP_α** and **BFP_β** crystallized by CH-π interaction and exhibited almost the same conformation and packing. Thus, the crystal morphologies or PL characteristics were not different from each other. Therefore, the effect of fluorination toward drastic change in packing motif was revealed as discussed for **BFTFP_α**, **BFTFP_β**, and **BFTFP_γ**, respectively.

Fig. S30 shows the crystal structure of **PETFP**. The distance between the neighboring vinylene units was estimated to be 3.809 Å. According to the literature, the reaction between two vinylene units occurs even in the solid state of the molecules.[42] To discuss the effectivity of the oxygen-bridging strategy of **BFTFP**, photostability was compared between **BFTFP_α** and **PETFP**. Fig. S31 shows PL spectra at each UV irradiation time measured for an isolated crystal of **BFTFP_α** and **PETFP**, respectively (Excitation: λ = 365 nm). The PL intensity from **BFTFP_α** hardly decreased while that measured for **PETFP** almost disappeared. The origin of this low optical durability was attributed to the reaction between neighboring vinylenes. Thus, it was revealed that the oxygen bridging strategy plays an important role in increasing the photostability.

Experimental

Chemicals

Palladium(II) acetate (Wako), tris-(dibenzylideneacetone)dipalladium(0) (Pd_2dba_3; Sigma-Aldrich),

2-dicyclohexylphosphino-2',6'-dimethoxybiphenyl (S-Phos; Sigma-Aldrich), 1,4-dibromotetrafluorobenzene(TCI), 1,4-dibromobenzene (TCI), benzofuran-2-boronic acid (TCI), benzo[b]thiophene-2-boronic acid (TCI), (*E*)-styrylboronic acid (TCI) were used as received. All solvents were used as received.

Synthesis

Synthesis of 1,4-bis(benzofuran-2-yl)-2,3,5,6-tetrafluorophenylene (***BFTFP***): 1,4-Dibromotetrafluorobenzene (310 mg, 1.0 mmol), benzofuran-2-boronic acid (358 mg, 2.2 mmol), palladium(II) acetate (14 mg, 0.06 mmol), S-Phos (43 mg, 0.10 mmol), and stir chip were put in a 10 mL two-neck flask. The atmosphere of the flask was replaced with argon, then 2 mL of toluene and 2 mL of 2 M K_2CO_3 aq. were injected. The reaction was performed by heating at 100 °C under stirring for 42 hours. After that, the solvent was evaporated, and extraction was performed for the remaining solid using distilled 50 mL of water and 90 mL of chloroform in a 200 mL separation funnel. After gathering the chloroform phase, the solution was dried over $MgSO_4$. After filtration to remove $MgSO_4$, the solution was concentrated and purified by short-column chromatography using SiO_2 and chloroform. After evaporating the solvent, the obtained solid was dissolved in a small amount of chloroform in a one-neck flask to prepare the saturated chloroform solution. Next, 50 mL of methanol as a poor solvent was quietly mounted on the solution to perform crystal growth by a solvent diffusion process. To perform recrystallization, the flask was soon placed in a refrigerator (10 °C) under the dark for 17 hours. After that, white solids precipitated on the bottom of the flask and obtained the solid by filtration and following washing with methanol. The solid obtained on the filter paper was dried over 5 hours, yielding a white crystalline solid (142 mg, 0.37 mmol, 37 %). ^{1}H-NMR (400 MHz, $CDCl_3$): δ (ppm) 7.69 (d, 2H, *J* = 7.8 Hz), 7.62 (d, 2H, *J* = 8.2 Hz), 7.42-7.38 (m, 4H), 7.31 (t, 2H, *J* = 8.0 Hz); ^{13}C NMR (100 MHz, $CDCl_3$) δ (ppm) 155.1(C), 144.2(C) 127.9(C), 126.2(C), 123.6(C), 121.8(C), 111.7(C), 110.9(C); HR-MS (APCI/TOF) m/z: $[M + H]^+$ calculated for $C_{22}H_{10}F_4O_2$ 383.0690, found: 383.0710. (Figs S1-S3)

Synthesis of 1,4-bis(benzothiophene-2-yl)-2,3,5,6-tetrafluorophenylene (***BTTFP***): 1,4-Dibromotetrafluorobenzene (305 mg, 1.0 mmol), benzo[b]thiophene-2-boronic acid (392 mg, 2.2 mmol), palladium(II) acetate (13 mg, 0.06 mmol), S-Phos (41 mg, 0.10 mmol), and stir chip were put in a 10 mL two-neck flask. The atmosphere of the flask was replaced with argon, then 5 mL of toluene and 2 mL of 2 M K_2CO_3 aq. were injected. The reaction was performed by heating at 100 °C under stirring for 53 hours. After that, a solvent was evaporated, and extraction was performed for the remaining solid using distilled 50 mL of water and 100 mL of chloroform in a 200 mL separation funnel. After gathering the chloroform phase, the solution was concentrated. Next, 100 mL of methanol as a poor solvent was quietly mounted on the solution to perform crystal growth by a solvent diffusion process. To perform recrystallization, the flask was soon placed in a refrigerator (10 °C) in the dark for 30 minutes. After that, white solids precipitated on the bottom of the flask and obtained the solid by filtration and following washing with methanol. Next, all solids were dissolved in 50 °C of chloroform and then filtered using a filter paper. After cooling at room temperature, 100 mL of methanol as a poor solvent was quietly mounted on the solution to perform crystal growth by a solvent diffusion process. To perform recrystallization, the flask was soon placed in a refrigerator (10 °C) under the dark for 5 hours. After that, white solids precipitated on the bottom of the flask and obtained the solid by filtration and following washing with methanol. The obtained solids were then dried under vacuum for 3 hours, yielding a white crystalline solid (109 mg, 0.26 mmol, 26 %). ^{1}H-NMR (400 MHz, $CDCl_3$): δ (ppm) 7.85-7.95 (m, 6H), 7.38-7.46 (m, 4H); ^{13}C NMR (100 MHz, $CDCl_3$) δ (ppm) 193.3 (C), 139.0(C) 128.0(C), 127.6(C), 125.7(C), 124.8(C), 124.5(C), 122.0 (C); HRMS (APCI/TOF) m/z: $[M + H]^+$ calculated for $C_{22}H_{10}F_4S_2$ 415.0233, found: 415.0239. (Figs S12-S14)

Synthesis of 1,4-bis(benzofuran-2-yl)-phenylene (***BFP***): 1,4-Dibromobenzene (199 mg, 0.6 mmol), benzofuran-2-boronic acid (233 mg, 1.4 mmol), palladium(II)acetate (14 mg, 0.66 mmol), S-Phos (49 mg, 0.10 mmol), and stir chip were put in a 50 mL two-neck flask. The atmosphere of the flask was replaced with argon, then, 8 mL of toluene and 8 mL of 2 M K_2CO_3 aq. were injected. The reaction was performed by heating at 100 °C under stirring for 46 hours. After that, a solvent was evaporated, and extraction was performed for the remaining solid using distilled 150 mL of water and a total of 150 mL of chloroform in a 200 mL separation funnel. After gathering the chloroform phase, the solution was dried over $MgSO_4$. After filtration to remove $MgSO_4$, the solution was concentrated to prepare a saturated chloroform solution. Next, 140 mL of methanol as a poor solvent was quietly mounted on the solution to perform crystal growth by a solvent diffusion process. To perform recrystallization, the flask was soon placed in a refrigerator (10 °C) under the dark for 24 hours. After that, white solids precipitated on the bottom of the flask and obtained the solid by filtration and following washing with methanol. The solid obtained on the filter paper was dried over 5 hours, yielding a white crystalline solid (73 mg, 0.23 mmol, 38 %). ^{1}H NMR (400 MHz, CD_2Cl_2): δ (ppm) 7.97 (s, 4H), 7.63 (d, 2H, *J* = 7.3 Hz), 7.55 (d, 2H, *J* = 8.2 Hz), 7.32 (t, 2H, *J* = 7.5 Hz), 7.26 (t, 2H, *J* = 7.3 Hz), 7.15 (s, 2H); ^{13}C NMR (100 MHz, $CDCl_3$) δ (ppm) 155.5(C), 155.1(C) 130.5(C), 129.3(C), 125.4(C), 124.7(C), 123.2(C), 121.1(C) 111.4(C), 102.1(C); HRMS (APCI/TOF) m/z: $[M + H]^+$ calculated for $C_{22}H_{14}O_2$ 311.10, found: 311.1066. (Figs S15-S16)

Synthesis of trans,trans-1,4-bis(2-phenylethenyl)-2,3,5,6-tetrafluorophenylene (***PETFP***): 1,4-Dibromotetrafluorobenzene (154 mg, 0.5 mmol), (*E*)-styrylboronic acid (163 mg, 1.1 mmol), Pd_2dba_3 (4.6 mg, 0.005 mmol), S-Phos (8.2 mg, 0.02 mmol), and stir chip were put in a 50 mL two-neck flask. The atmosphere of the flask was replaced with argon, then, 20 mL of toluene and 8 mL of 2 M K_2CO_3 aq. were injected. The reaction was performed by heating at 100 °C under stirring for 64 hours. After that, extraction was performed for the reaction solution using distilled 100 mL of water and a total of 150 mL of chloroform using a 200 mL separation funnel. After gathering the chloroform phase, the solution was dried over $MgSO_4$. After filtration to remove $MgSO_4$, the solution was concentrated and purified by short-column chromatography using SiO_2 and chloroform. After evaporating solvent, the obtained solid was

dissolved in 20 mL of chloroform in a 200 mL one-neck flask. Next, 60 mL of methanol as a poor solvent was quietly mounted on the solution to perform crystal growth by a solvent diffusion process. To perform recrystallization, the flask was soon placed in a refrigerator (10 °C) under the dark for 8 hours. After that, white solids precipitated on the bottom of the flask and obtained the solid by filtration and following washing with methanol. The solid obtained on the filter paper was dried over 8 hours, yielding a white crystalline solid (132 mg, 0.37 mmol, 74 %). ^{1}H-NMR (400 MHz, $CDCl_3$): δ (ppm) 7.57-7.50 (m, 6H), 7.40 (t, 4H, *J* = 7.3 Hz), 7.33 (t, 2H, *J* = 7.1 Hz,), 7.10 (d, 2H, *J* = 16.9 Hz); ^{13}C NMR (100 MHz, CDCl3) δ (ppm) 146.1(C), 143.6(C) 137.2(C), 136.9(C), 129.0(C), 127.1(C), 115.2(C), 114.2(C); HRMS (APCI/TOF) m/z: $[M + H]^+$ calculated for $C_{22}H_{14}F_4$ 355.10, found: 355.1106. (Figs S18-S20)

Crystal growth

Solvent diffusion process: 0.5 mg/mL – 1.0 mg/mL of dichloromethane solution was prepared for each molecule. 10 mL of the solution was injected in a 20 mL vial. Next, 10 mL of methanol was quietly mounted onto the solution to perform the crystal growth by solvent diffusion process. After capping the vial, the solution remained at room temperature until methanol was perfectly penetrated in the dichloromethane phase.

Vapor diffusion process: 0.5 mg/mL – 1.0 mg/mL of dichloromethane solution was prepared for each molecule. 7 mL of the solution was injected into a glass petri dish (AS ONE, FS-90B) containing a cut glass plate (Matsunami Glass Ind. Ltd., S1214). The petri dish was confined in a glass bell jar (Kiriyama Glass Co., VKB-200). To perform the vapor diffusion process, 20 mL of methanol was also confined in the glass bell jar. The equipment remained for several hours until almost all solvents in the petri dish evaporated.

Sublimation process: Here, one of the typically utilized methods is described. First, *ca.* 5 mg of molecular powder was placed inside a glass pipet (Sansyo Co. Ltd., disposable Pasteur pipet: *φ*7×230mm). The pipet containing the powder was heated at 300 °C for a few minutes for crystal growth by sublimation. The heating process was performed using a heating stage (MSA Factory Co. Ltd., PA3003). The crystals were obtained from the opposite inner surface of the glass pipet.

Measurements

Unless otherwise noted, all the experiments were conducted at room temperature (25 ± 3 °C). Liquid-state ^{1}H (400 MHz) and ^{13}C (100 MHz) nuclear magnetic resonance (NMR) spectra were recorded on a JEOL ECZ400S. Chemical shifts (δ) were expressed relative to the resonances of the residual non-deuterated solvents for ^{1}H [$CDCl_3$:^{1}H(δ) = 7.26 ppm] or ^{1}H [CD_2Cl_2: ^{1}H(δ) = 5.33 ppm] and ^{13}C [$CDCl_3$: ^{13}C(δ) = 77.16 ppm]. Absolute values of the coupling constants were given in Hertz (Hz), regardless of their sign. Multiplicities were abbreviated as singlet (s), doublet (d), triplet (t), and multiplet (m). Mass spectral analysis was performed by compact QTOF (Bruker) and the data was analyzed with DataAnalysis 5.1. Data collection for X-ray crystal analysis was performed on Rigaku/XtaLAB Synergy-S/Cu (Mo−Kα λ = 0.7107 Å) diffractometers. The X-ray measurement was performed at −170 °C or -160 °C. The structures were solved by direct methods (SHELXT) and refined through full-matrix least-squares techniques on F^2 using SHELXL and OLEX2 crystallographic software packages. PL and those excitation spectra were measured on a JASCO model FP-8500 spectrophotometer. Absolute quantum yield (Φ_{PL}) was estimated by Hamamatsu C9920-02 equipped with an integrating sphere. The spectra used for the estimation of ΦPL were included in Appendix 1 in the supporting information file. Optical microscope fluorescence images were obtained by SHIMADZU moticam 1080BMH with WUBEN E19 UV 365 nm. WUBEN E19 was also used for the examinations of photostability. Spatially resolved μ-PL spectra were measured by an analyzing system [405 nm UV laser OptoSigma LDU33-405-3.5 (Sigma-Koki), micro-PL spectra using a USB400 and a R200-7-UV−vis probe recorded by a CCD (detector: Sony ILX511B linear siliconCCD array). The excitation laser was filtered with a band-pass filter (YIF-BA460IFS) and focused on the crystal samples with an objective lens (50×, NA = 0.80 or 20×, NA = 0.45). The crystal samples were excited at 5.0 μW. The collected emission was then guided to a spectrometer (Lambda Vision SA-100A) and recorded by a CCD (detector: Hamamatsu Photonics S11151-2048 CCD linear image sensor). Optically pumped lasing was measured using a fiber-coupled spectrometer (HRS-300S-NI-KKAS) equipped with a CCD detector (PIXIS-256E-KKAS), and a Nd:YAG laser ($\lambda_{3\omega}$ = 355 nm, > 5 ns pulse duration, 1 kHz repetition) as an optical excitation source. Crystal thickness was measured using a surface profiler (KLA-Tencor, Alpha-Step D-500).

Theoretical calculations

Density functional theory (DFT) calculation was performed using the Gaussian 03 suite of programs using the B3LYP/6-31G + methods. The orbital diagrams were generated using the GaussView program.[56]

Conclusions

We newly designed a highly luminescent, and polymorphic compound, **BFTFP**. Polymorphs with drastically varied morphologies, and crystal structures were obtained due to the modified crystal growth methodologies. Owing to the variations of crystal structures of **BFTFP**, specific photonic functions relating to the flexible fluorescence waveguiding, ASE, and vertical cavity resonators were successively assigned for each polymorph. The effectivity was also supported by comparison to crystals of similar chemical structures.

Author contributions

T.M. designed the research, performed experiments, and wrote the manuscript. S.H. supervised these processes.

Conflicts of interest

There are no conflicts to declare.

Data availability

A data availability statement (DAS) is required to be submitted alongside all articles. Please read our full guidance on data availability statements for more details and examples of suitable statements you can use.

Acknowledgements

S. H. acknowledges the JST FOREST Program (no. JPMJFR211W) and a KAKENHI (Grant-in-Aid for Scientific Research B: no. 24K01574) of the Japan Society for the Promotion of Science (JSPS). T. M. acknowledges a KAKENHI (Grant-in-Aid for Young Scientific Research: no. 22K14671), and a Scientific Research Grant from "Iketani Science and Technology Foundation". The authors acknowledge Prof. Dr. Akitaka Ito at Kochi University of Technology for measurements of PL lifetime and evaluation of Φ_{PL}. The acknowledge also goes to Mr. Nakabayashi and Mr. Shimada at Kochi University of Technology for the measurements and analysis of MS spectra.

Notes and references

1 S. Sandanayaka, T. Matsushima, F. Bencheikh, S. Terakawa, W. J. Potscavage Jr, C. Qin, T. Fujihara, K. Goushi, J. Ribierre and C. Adachi, *Appl. Phys. Express*, 2019, **12**, 061010.
2 K. Yoshida, J. Gong, A. L. Kanibolotsky, P. J. Skabara, G. A. Turnbull and I. D. W. Samuel, *Nature* 2023, **621**, 746–752.
3 K. Takimiya, K. Bulgarevich, M. Abbas, S. Horiuchi and T. Ogaki, K. Kawabata and A. Ablat, *Adv. Mater.* 2021, **33**, 2102914.
4 T. He, M. Stolte, C. Burschka, N. H. Hansen, T. Musiol, D. Ka¨lblein, J. Pflaum, X. Tao, J. Brill and F. Wu¨rthner, *Nat. Commun* 2015, **6**, 5954.
5 T. Kanagasekaran, H. Shimotani, K. Kasai, S. Onuki, R. D. Kavthe, R. Kumashiro, N. Hiroshiba, T. Jin, N. Asao and K. Tanigaki, arXiv:1903.08869.
6 J. Gierschner, S. Varghese and S. Y. Park, *Adv. Optical. Mater.* 2016, **4**, 348−364.
7 H. Huang, Q. Zheng, B. Yu, Y. Yang, Y. Li, Y. Li, Y. Ji, Q. Liao, and H. Fu, *J. Phys. Chem. Lett.* 2024, **15**, 4890−4897.
8 H.-H. Fang, R. Ding, S.-Y. Lu, Y.-D. Yang, Q.-D. Chen, J. Feng, Y.-Z. Huang and H.-B. Sun, *Laser Photonics Rev.* 2013, **7**, 281–288.
9 T. Matsuo, Y. Ueda, H. Mizuno, F. Sasaki, K. Yamashita and H. Yanagi, *ACS Photonics* 2022, **9**, 2015-2023.
10 J. Tang, J. Zhang, Y. Lv, H. Wang, F. F. Xu, C. Zhang, L. Sun, J. Yao and Y. S. Zhao, *Nat Commun* **2021**, 12, 3265.
11 T. Matsuo, F. Sasaki and H. Yanagi, *Appl. Phys. Express* 2022, **15**, 051002.
12 T. Matsuo and S. Hayashi, *J. Phys. Chem. Lett.*, 2024, **15**, 3968−3974.
13 T. Matsuo, S. Azuma, M. Nakabayashi, F. Sasaki and S. Hayashi, *Adv. Optical Mater.* 2025, 2402701.
14 T. Matsuo, C. Rössiger, J. Herr, R. Göttlich, D. Schlettwein, H. Mizuno, F. Sasaki and H. Yanagi, *RSC Adv.*, 2020, **10**, 24057.
15 S. Chen, X.-D. Wang, M.-P. Zhuo, G.-Q. Wei, J.-J. Wu and L.-S. Liao, *Adv. Optical Mater.* 2022, **10**, 2101931.
16 H. Liu, Z. Lu, B. Tang, Z. Zhang, Y. Wang and H. Zhang, *Dyes. Pigm.* 2018, **149**, 284–289.
17 R. Huang, Y. Wang, Y. Huang, M. Wang and S. Liao, *Dyes Pigm.* 2025, **235**, 112639.
18 Y. Tanaka, K. Goto, K. Yamashita, T. Yamao, S. Hotta, F. Sasaki and H. Yanagi, *Appl. Phys. Lett.* 2015, **107**, 163303.
19 S. M. Yoon, J. Lee, J. H. Je, H. C. Choi and M. Yoon, *ACS Nano* 2011, **5**, 2923–2929.
20 S. Zhao, H. Yamagishi, O. Oki, Y. Ihara, N. Ichiji, A. Kubo, S. Hayashi and Y. Yamamoto, *Adv. Optical Mater.* 2022, **10**, 2101808.
21 T. Matsuo, J. Kuwabara, T. Kanbara and S. Hayashi, *J. Phys. Chem. Lett.* 2023, **14**, 6577−6582.
22 X. Feng, R. Lin, S. Yang, Y. Xu, T. Zhang, S. Chen, Y. Ji, Z. Wang, S. Chen, C. Zhu, Z. Gao and Y. S. Zhao, *Angew. Chem. Int. Ed.* 2023, **62**, e202310263.
23 T. Yamao, Y. Taniguchi, K. Yamamoto, T. Miki, S. Ota, S. Hotta, M. Goto and R. Azumi, *Jpn. J. Appl. Phys.* 2007, 46, 7478–7482.
24 M. Nakabayashi, T. Matsuo, S. Hayashi, *Chem. Eur. J.* 2023, **29**, e2023023.
25 K. Takazawa, J. Inoue, K. Mitsuishi and T. Takamasu, *Adv. Mater.* 2011, **23**, 3659–3663.
26 J. Ravi and R. Chandrasekar, *Adv. Optical Mater.* 2021, **9**, 2100550.
27 S. Hayashi, S. Yamamoto, D. Takeuchi, Y. Ie and K. Takagi, *Angew. Chem. Int. Ed.* 2018, **57**, 17002.
28 X. Cao, J. Peng, W. Wang, W. Xu, S. Xu, Dyes. Pigm. 2023, **219**, 111531.
29 Z. Lu, Y. Zhang, H. Liu, K. Ye, W. Liu and H. Zhang, *Angew. Chem. Int. Ed.* 2020, **59**, 4299 –4303.
30 L. Catalano, D. P. Karothu, S. Schramm, E. Ahmed, R. Rezgui, T. J. Barber, A. Famulari and P. Naumov, *Angew. Chem. Int. Ed.* 2018, **57**, 17254 –17258.
31 H. Liu, Z. Bian, Q. Cheng, L. Lan, Y. Wang and H. Zhang, *Chem. Sci.* 2019, **10**, 227–232.
32 Y. Wu, J. Feng, X. Jiang, Z. Zhang, X. Wang, B. Su and L. Jiang, *Nat. Commun.* 2015, **6**, 6737.
33 M.-P. Zhuo, J.-J. Wu, X.-D. Wang, Y.-C. Tao, Y. Yuan and L.-S. Liao, *Nat. Commun.* 2019, **10**, 3839.
34 J. M. Halabi, E. Ahmed, L. Catalano, D. P. Karothu, R. Rezgui and P. Naumov, *J. Am. Chem. Soc.* 2019, **141**, 14966−14970.
35 M. Annadhasan, A. V. Kumar, P. Giri, S. Nandy, M. K. Panda, K. V. J. Jose and R. Chandrasekar, *Angew. Chem. Int. Ed.* 2023, **62**, e202302929.
36 M. Rohullah, V. V. Pradeep, S. Singh and R. Chandrasekar, *Nat. Commun.* 2024, **15**, 4040.
37 S. Hayashi and T. Koizumi, *Angew. Chem. Int. Ed.* 2016, **55**, 2701-2704.
38 T. Seki, N. Hoshino, Y. Suzuki and S. Hayashi, *CrystEngComm* 2021, **23**, 5686-5696.
39 T. Matsuo, K. Ikeda and S. Hayashi, *Aggregate*, 2023, **4**, e378.
40 Y. Oyama, M. Mamada, A. Shukla, E. G. Moore, S.-C. Lo, E. B. Namdas and C. Adachi, *ACS Materials Lett.* 2020, **2**, 161−167.
41 X. Zhu, H. Tsuji, J. T. L. Navarrete, J. Casado and E. Nakamura, *J. Am. Chem. Soc.* 2012, **134**, 19254−19259.
42 G. W. Coates, A. R. Dunn, L. M. Henling, J. W. Ziller, E. B. Lobkovsky and R. H. Grubbs, *J. Am. Chem. Soc.* 1998, **120**, 3641-3649.
43 H. Wang, P. Chen, Z. Wu, J. Zhao, J. Sun and R. Lu, *Angew. Chem.* 2017, 129, 9591 –9595.
44 G. J. O. Beran, I. J. Sugden, C. Greenwell, D. H. Bowkill, C. C. Pantelides and C. S. Adjiman, *Chem. Sci.* 2022, **13**, 1288–1297.
45 E. Parisi, E. Santagata, E. Simone, F. Borbone and R. Centore, *J. Am. Chem. Soc.* 2024, **146**, 19405−19413.
46 G. H. Roche, D. Flot, J. J. E. Moreau, O. J. Dautel, J.-S. Filhol and A. Lee, *Cryst. Growth Des.* 2021, **21**, 3850−3863.
47 E. J. Wu, A. W. Kelly, L. Iuzzolino, A. Y. Lee and X. Zhu, *Angew. Chem. Int. Ed.* 2024, **63**, e202406214.
48 S. Ye, G. Liu, S. Pu and J. Wu, *Org. Lett.* 2012, **14**, 70-73.
49 Bernstein, J.; Polymorphism in Molecular Crystals; Oxford University Press: New York, **2002**.
50 C. Liu, J. G. Brandenburg, O. Valsson, K. Kremer, T. Bereau, *Soft Matter*, **2020**, *16*, 9683–9692.
51 S. K. Cohen and S. Forrest, *Nat. Photon* 2010, **4**, 371–375.

52 K. Yamashita, T. Nakahata, T. Hayakawa, Y. Sakurai, T. Yamao, H. Yanagi and S. Hotta, *Appl. Phys. Lett.* 2014, **104**, 253301.
53 O. Gidron, N. Varsano, L. J. W. Shimon, G. Leitus and M. Bendikov, *Chem. Commun.* 2013, **49**, 6256—6258.
54 P. A. Praveen, T. Kanagasekaran, C. Ma, M. Terada, T. Jin, Y. Wakabayashi and H. Shimotani, *J. Mater. Chem. C* 2024, **12**, 15995–16003.
55 P. A. Praveen, P. Muthuraja, P. Gopinath and T. Kanagasekaran, *J. Phys. Chem. A* 2022, **126**, 600−607.
56 M. J. Frisch, G. W. Trucks, H. B. Schlegel, G. E. Scuseria, M. A. Robb, J. R. Cheeseman, J. A. Montgomery Jr., T. Vreven, K. N. Kudin, J. C. Burant, J. M. Millam, S. S. Iyengar, J. Tomasi, V. Barone, B. Mennucci, M. Cossi, G. Scalmani, N. Rega, G. A. Petersson, H. Nakatsuji, M. Hada, M. Ehara, K. Toyota, R. Fukuda, J. Hasegawa, M. Ishida, T. Nakajima, Y. Honda, O. Kitao, H. Nakai et al. Gaussian 03, Revision C.02, Gaussian, Inc., Wallingford, CT 2004.

Note: The spectra used for the estimation of Φ_{PL} were included in the Appendix in the supporting information file.

The data supporting this article have been included as part of the Supplementary Information.

Crystallographic data has been deposited at the CCDC under 2420271 and can be obtained from https://www.ccdc.cam.ac.uk/structures/Search?Ccdcid=2420271&DatabaseToSearch=Published

Crystallographic data has been deposited at the CCDC under 2420272 and can be obtained from https://www.ccdc.cam.ac.uk/structures/Search?Ccdcid=2420272&DatabaseToSearch=Published

Crystallographic data has been deposited at the CCDC under 2420273 and can be obtained from https://www.ccdc.cam.ac.uk/structures/Search?Ccdcid=2420273&DatabaseToSearch=Published

Crystallographic data has been deposited at the CCDC under 2420274 and can be obtained from https://www.ccdc.cam.ac.uk/structures/Search?Ccdcid=2420274&DatabaseToSearch=Published

Crystallographic data has been deposited at the CCDC under 2420275 and can be obtained from https://www.ccdc.cam.ac.uk/structures/Search?Ccdcid=2420275&DatabaseToSearch=Published

Crystallographic data has been deposited at the CCDC under 2420276 and can be obtained from https://www.ccdc.cam.ac.uk/structures/Search?Ccdcid=2420276&DatabaseToSearch=Published

Crystallographic data has been deposited at the CCDC under 2420277 and can be obtained from https://www.ccdc.cam.ac.uk/structures/Search?Ccdcid=2420277&DatabaseToSearch=Published